ELSEVIER

Contents lists available at ScienceDirect

Additive Manufacturing

journal homepage: www.elsevier.com/locate/addma





Filament formation mechanisms in yield-stress fluid-enabled embedded ink writing

Weijian Hua^{a,1}, Cheng Zhang^{a,b,1}, Kellen Mitchell^a, Lily Raymond^a, Ryan Coulter^a, Erick Bandala^a, Danyang Zhao^{b,*}, Yifei Jin^{a,*}

ARTICLE INFO

Keywords: Filament formation Yield-stress fluid Embedded ink writing Filament evaluation system 3D structure printing

ABSTRACT

Embedded ink writing (EIW), an emerging material extrusion-based three-dimensional (3D) printing strategy, has demonstrated great potential for diverse applications. EIW consists of three key components: support bath, ink, and printing conditions. Filament formation in EIW is significantly affected by the coupling effects of these components, which is still unclear. This work aims to fundamentally unveil the filament formation processes and mechanisms within support bath materials with various rheological properties. A broader range of path speed is utilized to ensure the formation of diverse representative filaments from low- and high-viscosity hydrogel inks. By varying the combination of support bath, ink, and printing conditions, ten types of filaments are observed during EIW and their formation mechanisms are explained in detail. Particularly, when designing a support bath for EIW, thixotropic time serves as the baseline to determine the functionality of the bath. A relatively long thixotropic time can facilitate the formation of well-defined filaments. In addition, the support bath's yield stress decides the allowed maximum path speed. High yield stress is necessary if path speed is targeted in a higher range. Based on the experimental findings, a position-shape-size evaluation system is established and proposed for comprehensively evaluating printed filaments, which is helpful in filtering suitable filaments for EIW. Finally, complex 3D structures including a human nose and a human ear are printed at a high speed within the support bath with suitable rheological properties to bridge the gap between filament formation mechanisms and practical 3D printing applications.

1. Introduction

Embedded ink writing (EIW), one subcategory of material extrusion-based three-dimensional (3D) printing technology, has received significant attention in recent years [1–4] and has been widely applied in different fields, like soft robotics [5,6], wearable devices [7,8], and tissue engineering [9,10], etc. In this technology, a dispensing nozzle moves within a liquid support bath to print ink material into a pre-defined 3D structure, as shown in Fig. 1A. After printing, the 3D structure is solidified in and collected from the support bath. Because the liquid bath can provide omnidirectional supports to stabilize the deposited features, EIW is particularly suitable for printing 3D soft structures with complex geometries, which are challenging to fabricate via other material extrusion-based printing methods.

Support bath materials can be divided into two categories: hydrophobic and hydrophilic. Currently, hydrophobic baths, such as silicone oil-based ones, are commonly used to print hydrophobic ink materials [11,12] in order to minimize the interfacial tension effects. Although hydrophilic support baths are compatible with both hydrophobic [13, 14] and hydrophilic inks [9,10], they are primarily applied to print hydrophilic ink materials, such as bioinks, because of their extraordinary cytocompatibility [4], showing a great potential for constructing human tissues and organs in the future. Among different hydrophilic support bath materials [2,4], yield-stress fluids [15–17] possess unimaginable potential for the EIW of complex 3D structures. When a nozzle moves in a yield-stress fluid, the shear stress around the nozzle is higher than the critical yield stress, which enables the fluid to present a liquid state. In contrast, when the nozzle moves away, the localized

^a Mechanical Engineering Department, University of Nevada Reno, Reno, NV 89557, USA

b State Key Laboratory of High-performance Precision Manufacturing, School of Mechanical Engineering, Dalian University of Technology, Dalian, Liaoning 116024, China

^{*} Corresponding authors.

E-mail addresses: zhaody@dlut.edu.cn (D. Zhao), yifeij@unr.edu (Y. Jin).

 $^{^{1}\,}$ These authors contributed equally to this work.

shear stress decreases below the yield stress, which makes the fluid switch to a solid-like state. Thus, the yield-stress fluids have many unique advantages for EIW, including self-healing behavior during nozzle moving and printing due to repeatable and rapid transition between liquid and solid-like states; solid-like behavior after printing to provide excellent *in situ* support; and physical and/or chemical stability when prepared with suitable solvents [4,9,16].

Although the yield-stress fluid facilitates the embedded printing process, its solid-liquid transition also provides a more sophisticated environment for filament formation in comparison with traditional direct ink writing methods [15,16,18]. Therefore, successfully performing EIW requires mutual coordination between support bath material, ink material, and printing conditions, as shown in Fig. 1B. Some studies have been conducted to unveil the filament formation process within a yield-stress fluid. For example, Muth et al. [19] found that support bath materials must possess a sufficiently high elastic modulus to support printed structures and an appropriate yield stress to allow a nozzle to move freely in a support bath. Grosskopf et al. [20] found that Oldroyd number, as a function of nozzle diameter, path speed, and composition of support bath material, was the key to control the yielded dimensions around a dispensing nozzle during printing. Friedrich et al. simulated filament extrusion in a yield-stress bath [21] and further recorded the filament formation in different nanoclay baths via a high-speed camera [22]. Jin et al. [23] pointed out that the mismatched rheological properties of inks and support bath materials resulted in the formation of various irregular filaments during yield-stress support bath-enabled 3D printing. However, these studies only focused on the effects of one or two key factors on filament printing, failing to explore the interrelationships between support bath material, ink material, and printing conditions. As a result, the filament formation mechanisms in EIW are still unclear. Additionally, there lacks a system to comprehensively evaluate whether a filament is suitable for EIW of complicated 3D structures.

This work aims to fundamentally unveil the filament formation processes within support bath materials with different rheological properties. A broader range of path speeds has been utilized to ensure the formation of diverse representative filaments from ink materials with high and low viscosities. Based on the experimental results, a filament evaluation system has been established in terms of filament position, shape, and size, which helps assess and filter suitable filaments for EIW. Finally, two complex 3D structures have been printed within the selected support bath with suitable rheological properties to validate the proposed theory from the manufacturing aspect.

2. Materials and methods

2.1. Ink material preparation

Two hydrogel inks with low and high viscosities were used in this study to print filaments, which were composed of sodium alginate (NaAlg) and polyethylene glycol diacrylate (PEGDA). For the ink preparation, deionized (DI) water was first added to the PEGDA stock solution to dilute it to the concentration of 15 % (v/v). An overhead stirrer (Thermo Fisher Scientific, Waltham, MA) was used to uniformly mix DI water and PEGDA at 300 rpm for 5 min at room temperature. After that, 0.1 % (w/v) photoinitiator I2959 (2-hydroxy-4'-(2-hydroxyethoxy)-2methylpropiophenone, Sigma-Aldrich, Burlington, MA) was added into the 15 % (v/v) PEGDA solution and mixed for 5 min. Then, dry NaAlg powder (NaC₆H₇O₆, Sigma-Aldrich, Burlington, MA) was dispersed into the solution at the concentrations of 3.0 and 7.0 % (w/v) to prepare the hydrogel inks with low and high viscosities, respectively. NaAlg powder was continuously mixed with the PEGDA solution using the overhead stirrer at 800 rpm for 40 min. Finally, the prepared hydrogel inks were degassed in a centrifuge (Cole-Parmer® VS3400, Cole Parmer Instrument Company, Vernon Hills, IL) at 2500 rpm for 2 min to remove bubbles and were stored in a sealed container before use. To improve the visibility, Nile blue A (Sigma-Aldrich, Burlington, MA) was added to the hydrogel inks at 0.01 % (w/v).

2.2. Support bath preparation

Based on the preliminary studies, six nanoclay-hydrogel nanocomposites with different rheological properties were selected, including 2 % (w/v) nanoclay-30 % (w/v) Pluronic F127, 2 % (w/v) nanoclay-1 % (w/v) Pluronic F127, 8 % (w/v) nanoclay-10 % (v/v) PEGDA, 6 % (w/v) nanoclay-10 % (v/v) PEGDA, 6 % (w/v) nanoclay-1 % (w/v) NaAlg, and 6 % (w/v) nanoclay-1.5 % (w/v) NaAlg. For the nanoclay-Pluronic F127 nanocomposites, nanoclay suspension was prepared first by dispensing dry nanoclay powder (Laponite® RD, Na_{0.7}Si₈Mg_{5.5}Li_{0.3}O₂₀(OH)₄, BYK Additives Inc., Gonzales, TX) into DI water at room temperature. The overhead stirrer was used to mix the powder with water at 600 rpm for at least 60 min until nanoclay was thoroughly hydrated. Then, Pluronic F127 powder (P2443, Sigma-Aldrich, Burlington, MA) was added to the suspension at 4 °C and mixed at this temperature using the overhead stirrer at 800 rpm until the resulting nanocomposite was clear and homogenous. For the nanoclay-PEGDA nanocomposites, PEGDA (Mn 700, Sigma-Aldrich, Burlington, MA) stock solution was diluted by DI water to the required concentration (i.e., 10 % (v/v)). The overhead stirrer was used at room

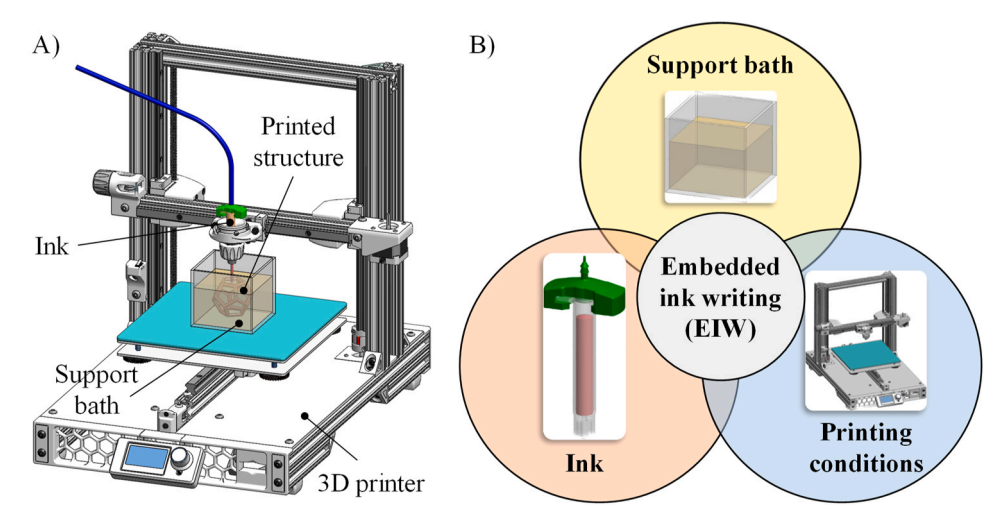


Fig. 1. A) Schematic of EIW. B) Three major factors in EIW: support bath material, ink material, and printing conditions.

temperature for mixing PEGDA and DI water at the speed of 300 rpm for 5 min. Then, nanoclay powder was added into the diluted solution at the given concentrations and mixed using the stirrer at the speed of 600 rpm for 60 min to prepare the nanocomposites. For the nanoclay-NaAlg nanocomposites, NaAlg powder was first dispersed into DI water and continuously mixed using the overhead stirrer (speed: 800 rpm and time: 40 min) to obtain the NaAlg solutions at 1 and 1.5 % (w/v). Then, dry nanoclay powder was dispersed into the solutions at 6 % (w/v) and mixed using the overhead stirrer at the speed of 600 rpm and time of at least 60 min. After preparation, all nanocomposites were degassed using the centrifuge at the speed of 2500 rpm for 2 min to remove air bubbles which were subsequently stored in the dark and sealed containers and aged for one day before use.

2.3. Rheological measurements

The zero-shear-rate viscosities (η_0) of two hydrogel inks were measured using a rheometer (MCR 92, Anton Paar, Ashland, VA) with a cone-plate measuring system (cone angle of 1°, cone diameter of 50.0 mm, and cone-to-plate gap of 0.102 mm). The steady shear rate sweeps were conducted to measure the viscosity change over shear rate ($\dot{\gamma}$) increasing from 0.01 to 1000 s⁻¹. The frequency sweeps were performed at a low strain of 1.0 % for the hydrogel inks to obtain the storage modulus (G') and loss modulus (G") at the frequency range of 0.1–10 Hz.

Two key rheological properties including yield stress (τ_0) and thixotropic time (t_c) of each nanocomposite were measured using the rheometer. The steady shear rate sweeps were conducted to measure the yield stress values. In the experiments, $\dot{\gamma}$ was increased from 0.01 to $1000~\rm s^{-1}$ and the shear stress (τ) was recorded. Based on the shear stress-shear rate curve, τ_0 was calculated using the Herschel-Bulkley model: $\tau=\tau_0+k\dot{\gamma}^n$, where k is the consistency index and n is the flow behavior index. The transient step shear rate sweeps were used to measure the thixotropic time of each nanocomposite. In the experiments, the nanocomposite sample was firstly pre-sheared at a relatively high shear rate of $10~\rm s^{-1}$ for $200~\rm s$. Then, the shear rate was decreased to a low value of $0.01~\rm s^{-1}$ for $1000~\rm s$. The variation of viscosity during this process was recorded. All the rheological measurements were performed at room temperature.

2.4. Experimental design of filament printing

The experimental setup for filament printing was illustrated in Fig. 2. The hydrogel ink was loaded into a syringe which was mounted to a homemade EIW 3D printing system modified based on a fused deposition modeling (FDM) printer (SOVOL 3D, Shenzhen Liandian Technology Co., Ltd., Shenzhen, China). A pressure control system (IP211-X120, Omega Engineering, Norwalk, CT) was applied to regulate the dispensing pressure (P) for pushing the ink out of a nozzle. A transparent container (acrylic container with a length of 4.3 in., width of 2.7 in., and height of 1 in., †Blulu, China) was used to pack each nanocomposite as the support bath. A camera (120fps USB camera, ELP, Shenzhen, China) was located to record the filament formation process from the back view. After printing, the filament inside the container was moved underneath a high-precision measurement system (VERTEX 251UC, Micro-Vu, Windsor, CA), which was an optical microscope with a high resolution, to observe the filament morphology/geometry from the top view. In the experiments, a 21-gauge nozzle (inner diameter $(2R_n)$: 0.51 mm and length (L_n) : 12.7 mm, EFD Nordson, Vilters, Switzerland) and a 25gauge nozzle ($2R_n$: 0.25 mm and L_n : 12.7 mm, EFD Nordson, Vilters, Switzerland) were used to deposit the filaments from different hydrogel inks. Specifically, 3 % (w/v) NaAlg-15 % (v/v) PEGDA was extruded at the dispensing pressure of 6 psi (41 kPa) using the 21-gauge nozzle and 10 psi (69 kPa) using the 25-gauge nozzle, respectively. 7 % (w/v) NaAlg-15 % (v/v) PEGDA was extruded at the dispensing pressure of 20 psi (138 kPa) using the 21-gauge nozzle and 40 psi (276 kPa) using

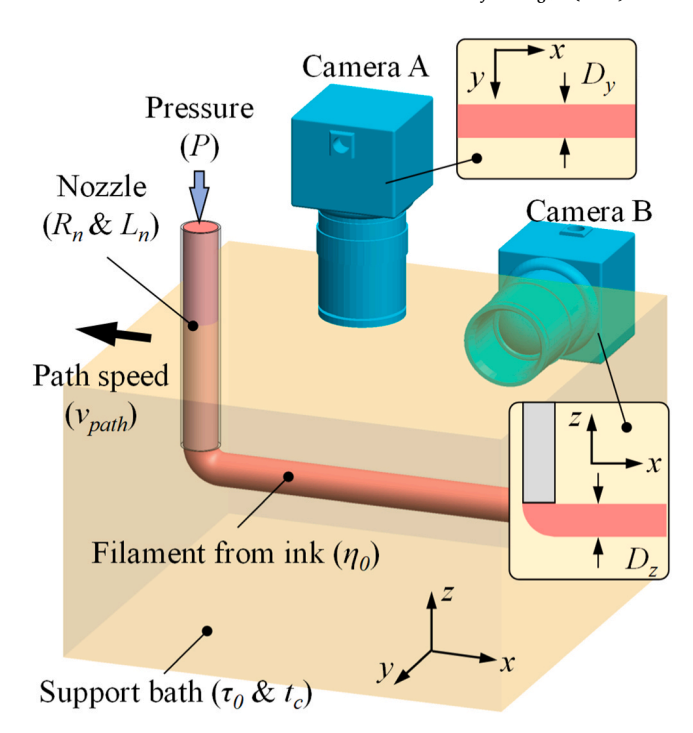


Fig. 2. Experimental setup for filament printing and characterization.

the 25-gauge nozzle, respectively. The path speed (ν_{path}) was increased from 0.3 to 3.0, 30.0, and 110.0 mm/s. The dimensions in the images were measured using ImageJ (https://imagej.nih.gov/ij/).

2.5. Embedded 3D printing of complex 3D structures

The hydrogel ink composed of 7 % (w/v) NaAlg and 15 % (v/v) PEGDA was used to print complex 3D structures within the support bath with 2.0 % (w/v) nanoclay and 30.0 % (w/v) Pluronic F127. The blue dye was also added to the hydrogel ink at 0.01 % (w/v) to enhance the visibility. The homemade 3D printing system was applied to print a human nose and an ear at room temperature. Before printing, the dispensing nozzle was carefully adjusted to make it perpendicular to the path speed direction. The printing parameters included the dispensing nozzle of 21-gauge ($2R_n$: 0.51 mm and L_n : 25.4 mm, EFD Nordson, Vilters, Switzerland), dispensing pressure of 50 psi, path speed of 110.0 mm/s, and step distance of 0.5 mm. The nose and ear models were directly downloaded from Sketchfab (https://sketchfab.com/) as the STL files. After printing, the structures inside the support bath were exposed to ultraviolet (UV) light offered by a UV curing system (OmniCure Series 2000, wavelength: 320-500 nm, Lumen Dynamics, Mississauga, ON, Canada) for 15 min and then moved into the refrigerator (4 °C) for 30 min to liquefy the nanocomposite. Finally, the nose and ear structures were collected from the support bath and submerged in a 2.0 % (w/v) calcium chloride (C8106, Sigma-Aldrich, Burlington, MA) solution for 1 h for ionic crosslinking.

2.6. Statistical analysis

All quantitative values of measurement in the figures were reported as means \pm standard deviation (SD) with n=3 samples per group.

3. Results and discussion

3.1. Characterization of ink materials and yield-stress fluids

In this work, the NaAlg-PEGDA hydrogel ink is selected for printing filaments within different yield-stress support baths, which has been

widely used for diverse biomedical applications. Particularly, the interactions between two components result in the formation of a semiinterpenetrating networked microstructure that improves the rheological and mechanical properties of the hydrogel ink [24,25]. Herein, NaAlg concentration is used to tune the ink's viscosity. The Carreau-Yasuda model: $\eta(\dot{\gamma})=\eta_{\infty}+\left(\eta_{0}-\eta_{\infty}\right)\left(1+\left(\lambda\dot{\gamma}\right)^{a}\right)^{(n-1)/a}$ is applied to calculate η_0 of each hydrogel ink as shown in Fig. S1A, where η_{∞} is the infinite viscosity, λ is the relaxation time, and a is the transition parameter. Both hydrogel inks present decreasing viscosities as the shear rate increases, exhibiting a typical shear-thinning behavior. The hydrogel ink with 3 % (w/v) NaAlg has a very low η_0 of approximately 0.72 Pa·s, which is comparable to that of collagen [26]. In contrast, the hydrogel ink with 7 % (w/v) NaAlg is much more viscous with the η_0 of 613.5 Pa·s. This is because the increase of NaAlg concentration leads to the existence of more alginate polymer chains in the hydrogel ink that densify the semi-interpenetrating networks formed with PEGDA polymer chains, making the hydrogel ink difficult to flow [27,28]. Since the calculated η_0 values cover the viscosity range of most of the inks for EIW [4,29], the filament formation results in this work are more representative. In addition, the frequency sweeps are conducted to explore the degree of fluid-like behavior in the hydrogel inks, as shown in Fig. S1B. At lower frequencies, G' of each hydrogel ink is higher than G'', which indicates the ink presents a solid-like behavior because the semi-interpenetrating network is not fully disrupted. When the frequency increases to a higher range, G'' exceeds G', demonstrating a behavior transition of the hydrogel ink from solid-like to fluid-like as the networked microstructure collapses at higher frequencies [24].

For the support bath materials, two key rheological parameters, i.e., yield stress and thixotropic time, are characterized. The former is used to quantify the robustness of formed microstructures within the nanocomposites at the microscale as well as to determine the capability of support bath for holding printed filaments at the macroscale [15,25]. The latter is commonly applied to evaluate the microstructure recovery time of a yield-stress fluid and assess the duration of the fluid to switch between liquid and solid-like states at the macroscopic level. Longer thixotropic time enables the liquefied support bath to fully fill the crevasse due to nozzle movement [25,30]. Herein, nanoclay is selected as the particle additive to tune the rheology of nanocomposites, which has the basic unit of nanoplatelet with negative charges on faces and positive charges on edge [16,31]. This charged characteristic not only allows nanoplatelets in an aqueous solvent to form a "house-of-cards" microstructure through electrostatic interactions [16,31], but also makes nanoclay miscible with diverse hydrogels to design nanocomposites with different rheological properties. In this work, Pluronic F127, PEGDA, and NaAlg are used as the hydrogel solvents to prepare the support baths with the yield stresses and thixotropic times falling into the representative ranges, as shown in Fig. S2.

According to the rheological findings, the nanoclay-Pluronic F127 nanocomposites exhibit a broad range of yield stress and thixotropic time values. The 2 % nanoclay-30 % Pluronic F127 nanocomposite has a high yield stress of 414.9 Pa and a long thixotropic time of 0.46 s, while the nanocomposite with 1 % Pluronic F127 has zero yield stress and a very short thixotropic time of 0.09 s, as shown in Fig. S2A and B, respectively. These changes are attributed to the micellization of Pluronic F127 phase in the nanocomposites, which is mainly affected by concentration at a given temperature [25,32]. Pluronic F127 is a triblock copolymer composed of poly(ethylene oxide) (PEO) and poly (propylene oxide) (PPO) species. At room temperature, Pluronic F127 has a critical micelle concentration of around 20 % (w/v) [33]. Below this concentration (e.g., 1 % (w/v)), each copolymer chain exists in a linear PEO-PPO-PEO configuration that attaches to nanoclay to shield the interactions between nanoplatelets [33]. Therefore, the "house-of-cards" microstructure from nanoclay collapses, making the nanocomposite lose its yield-stress property and become liquid. Since there is no well-organized microstructure within the nanocomposite, the

thixotropic time for microstructure recovery approaches to zero. Above this critical concentration (e.g., 30 % (w/v)), PEO-PPO-PEO species can form spherical micelles, which consist of a hydrophobic PPO core surrounded by a hydrophilic PEO corona [34]. Numerous micelles aggregate together to generate a jammed microstructure [34]. Simultaneously, the "house-of-cards" microstructure is regained because PEO-PPO-PEO species leave nanoplatelets. As a result, an interactive dual microstructure exits in the nanocomposite, increasing the threshold shear stress (i.e., τ_0) to break the microstructure as well as extending the time (i.e., t_c) to recover the microstructure after disturbance. These two nanoclay-Pluronic F127 nanocomposites are used in this study to represent support baths with (high τ_0 , long t_c) and (low τ_0 , short t_c), respectively. For the nanoclay-PEGDA nanocomposites, when the nanoclay concentration decreases from 8 % to 6 % (w/v), the nanocomposite's τ_0 decreases from 350.6 Pa to 174.9 Pa (Fig. S2A), while t_c increases from 0.07 to 0.12 s (Fig. S2B). The changes of τ_0 and t_c in the nanocomposites are consistent with the changes of those in the pure nanoclay suspensions [24,35], which validates that the interactions between nanoclay and PEGDA as well as their effects on the formed microstructure are negligible. As a result, both τ_0 and t_c of the nanoclay-PEGDA nanocomposites are mainly determined by nanoclay. Higher nanoclay concentration indicates a denser "house-of-cards" microstructure, which requires higher shear stress to disturb it but a shorter time for recovery. Thus, these two nanoclay-PEGDA nanocomposites are used in this work to represent support baths with (high τ_0 , short t_c) and (medium τ_0 , short t_c), respectively. The τ_0 and t_c of two nanoclay-NaAlg nanocomposites are illustrated in Fig. S2. The increase of NaAlg concentration from 1 % to 1.5 % (w/v) causes a significant decrease of τ_0 from 174.8 to 17.2 Pa and a slight decrease of t_c from 0.27 to 0.21 s. These changes can be explained by the interactions between nanoclay and NaAlg. Negatively charged alginate polymer chains can attach to nanoplatelets' edges with positive charges [36], which partially replace the electrostatic interactions between nanoplatelets, weakening the formed "house-of-cards" microstructure. Therefore, both τ_0 and t_c decrease in this NaAlg concentration range. These two nanoclay-NaAlg nanocomposites are utilized in this work to represent support baths with (medium τ_0 , long t_c) and (low τ_0 , long t_c), respectively.

3.2. Filament formation in different yield-stress support baths

The six nanoclay-hydrogel nanocomposites with different rheological properties are used as the representative support baths to investigate the filament formation mechanisms in a wider path speed range. EIW of low-viscosity ink (i.e., 3 % (w/v) NaAlg-15 % (v/v) PEGDA) is performed and the formed filaments are summarized in Fig. S3. As shown in Fig. 3A, both v_{path} and t_c affect the morphology of the extruded filament significantly. Specifically, compressed filaments [21,23] are generated at low path speeds (e.g., 0.3 and 3 mm/s), which have the dimension along the z direction (i.e., ink extrusion direction in Fig. 2) overwhelmingly larger than that along the y direction (i.e., the direction perpendicular to the nozzle moving direction in Fig. 2), as recorded in Movie S1. This filament formation mechanism is attributed to both the ink over-deposition in the support bath as well as the non-uniform compression from the support bath. Due to the ink's low η_0 , its extrusion speed (v_{ink}) is relatively high at the constant dispensing pressure (P)and nozzle geometries (R_n and L_n) based on Eq. (1) [23] as follows:

$$v_{ink} = \frac{P}{8\eta_0 L_n} R_n^2 \tag{1}$$

When ν_{path} is insufficient, more inks are deposited in the support bath around the nozzle tip, which results in the ink over-deposition. Simultaneously, the locally liquefied support bath material due to nozzle-induced shear stress can fill the crevasse behind the nozzle translation but needs a specific time duration to fully recovery its microstructure and yield stress at the macroscale, which leads to the non-uniform

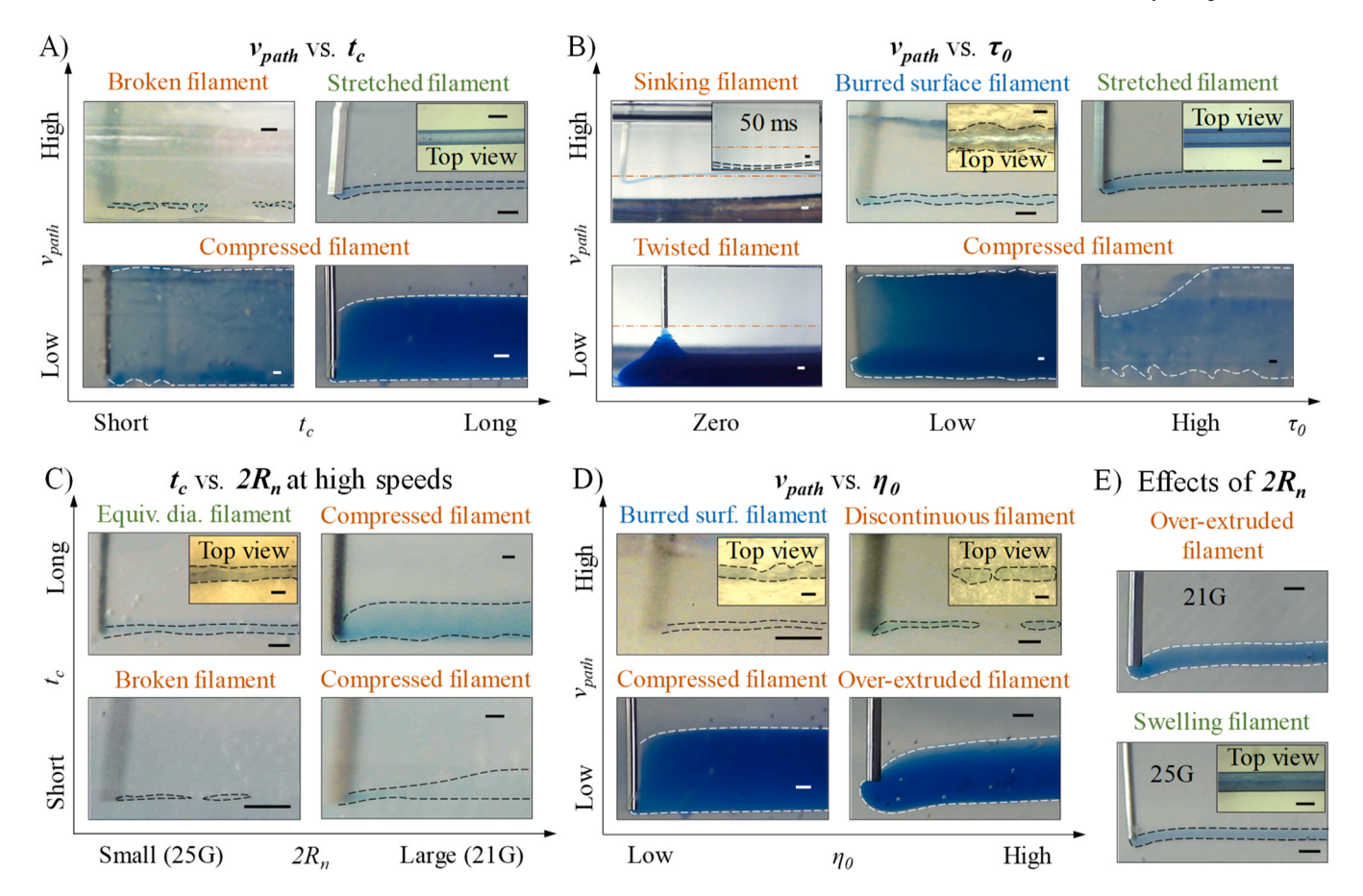


Fig. 3. Summary of filament formation within six representative support baths. Filament morphology as affected by A) v_{path} and t_c , B) v_{path} and τ_0 , C) t_c and $2R_n$ at high path speeds, D) v_{path} and η_0 , and E) $2R_n$. Scale bars: 1.0 mm for photos and 0.5 mm for insets.

compression [21,23]. As a result, the over-deposited ink with low viscosity is squeezed upwards until the localized support bath material regains the required yield-stress property. Similar phenomena are also observed in the support baths in Fig. S3B to 3E at the low path speeds. Specifically, when t_c is short, the support bath material behind the nozzle rapidly switches from liquid to solid-like state and cannot even fill the crevasse. In this scenario, the over-deposited ink may directly flow to the top surface of the support bath, as illustrated in Fig. 3A. When v_{path} increases to a higher range, the ink over-deposition can be effectively alleviated, resulting in the filaments with well-defined morphology within the support bath with long t_c . Particularly, when v_{path} (e.g., 110 mm/s) is much higher than v_{ink} , the dragging effect due to the speed difference functions, which causes the formation of stretched filament with a diameter smaller than the nozzle inner diameter, as illustrated in Fig. 3A and Movie S1. However, when printing in the support bath with short t_c , the bath's rapid liquid-to-solid-like transition makes the crevasse still exist. Simultaneously, the size of the extruded filament decreases greatly due to the dragging effect, which cannot overcome the surface tension between air and ink. As a result, the filament breaks up into segments (Movie S1) in the bath and is therefore named as broken filament.

Except t_c , τ_0 also affects the filament morphology, as illustrated in Fig. 3B. When printing in the support bath with high τ_0 , a stretched filament is generated at a higher path speed while a compressed filament is formed when the path speed decreases. In the low yield-stress support bath, a similar compressed filament can be created at a lower ν_{path} . However, controllable filaments are printable at higher ν_{path} . Although some burrs are generated on the filament (Fig. 3B and Movie S2) due to low τ_0 , these burred surface filaments still have acceptable overall shape and have been used in EIW to construct 3D structures with complex

geometries [9,37]. When the τ_0 of this support bath is negligible, the filament formation processes are unique, as shown in Fig. 3B. Because the bath's supporting capability is very poor, the extruded filaments twist spatially in the bath due to the ink over-deposition, especially at lower path speeds (as shown in Movie S2). This type of filament is named twisted filament and has also been observed in other published papers [23]. When v_{path} increases to the higher range, the extruded filaments are straightened by the fast nozzle movement. However, since the support bath cannot stably hold the filaments in situ, they move with the nozzle and sink gradually to the bottom of the support bath owing to the downward initial v_{ink} , as shown in Movie S2. This type of filament is therefore named as sinking filament [38]. These findings validate that ensuring sufficient yield stress has the highest priority when designing support bath materials for EIW, as it effectively eliminates disturbances from ink extrusion and nozzle movement that cannot be balanced solely by the support bath's buoyancy.

Supplementary material related to this article can be found online at doi:10.1016/j.addma.2024.104353.

After that, the same ink is extruded through the 25-gauge nozzle into the support baths to investigate the effects of $2R_n$ on the filament formation. The morphologies of the printed filaments are summarized in Fig. S4. Because the 25-gauge nozzle has an inner diameter smaller than that of the 21-gauge nozzle, based on Eq. (1), this change eventually causes a great decrease of v_{ink} , which makes the filament formation more controllable. As shown in Fig. 3C, only compressed filaments are generated within the baths with different t_c values, if the 21-gauge nozzle is applied. When the nozzle size is decreased to 25 gauge, a well-defined filament is generated within the bath with a long t_c , which has a diameter of around 240 μ m, close to the nozzle inner diameter of 250 μ m, as recorded in Movie S3. This filament is defined as equivalent

diameter filament [23,25] and can be used in EIW to make complex 3D structures. However, the decrease of v_{ink} makes the extruded filament size lower than the threshold value. As a result, broken filaments are generated within the bath with a short t_c , as shown in Fig. 3C and Fig. S4B.

Furthermore, the effects of ink's viscosity on filament formation are studied by depositing the high-viscosity ink (i.e., 7 % (w/v) NaAlg-15 % (v/v) PEGDA) into the support baths with different rheological properties. The filament morphologies are summarized in Fig. S5. The ink change increases η_0 significantly, as shown in Fig. S1A, which not only causes the decrease of v_{ink} based on Eq. (1) but also weakens the flowability of the ink. Additionally, the high-viscosity ink has better robustness than the low-viscosity ink [39,40], as validated in Fig. S1B. As a result, less ink material is extruded within the support bath at a low path speed, which expands along all directions, resulting in the formation of the over-extruded filament, as shown in Fig. 3D and Movie S4. This type of filament has a rough surface and uncontrollable overall shape that cannot be used for 3D printing applications. At a high path speed (e.g., 110 mm/s), filament breakup occurs in the support bath with low τ_0 and long t_c , even if the bath can completely fill the crevasse during nozzle translation, as recorded in Movie S4. The formation mechanism of this type of filament differs from that of broken filament. The surface tension effect is no longer the fundamental reason because there is no air-ink interface during filament extrusion. With the increase of path speed, the dragging effect becomes pronounced which drives the formation of stretched filament as well as residual tensile stress within the filament. Due to the low yield stress, the support bath cannot stably hold the filament in place, which gradually and non-uniformly shrinks to release the residual stress, eventually leading to filament segmentation. In order to be distinguished from broken filament in terms of formation mechanism, this type of filament is named as discontinuous filament.

Finally, the high-viscosity ink is extruded through the 25-gauge nozzle into different support baths to further validate the effects of nozzle inner diameter on filament formation. The formed filaments with various morphologies are summarized in Fig. S6. Because of higher η_0 and smaller $2R_n$, less ink material is extruded at a given time, as predicted by Eq. (1), which presents better shape controllability. Therefore, in the same support bath, an over-extruded filament is generated at 3 mm/s using the 21-gauge nozzle but a well-defined filament is formed through the 25-gauge nozzle, as shown in Fig. 3E. Specifically, this filament has a controllable overall shape as well as a diameter larger than the nozzle inner diameter, which is reported as swelling filament (as recorded in Movie S5) in other published papers [22,23] for 3D printing applications.

In summary, when designing a support bath for EIW, its rheological properties are comprehensively affected by ink properties (e.g., viscosity), printing conditions (e.g., path speed, nozzle diameter, dispensing pressure), and potential bath-ink interactions (e.g., interfacial tension [11,20]). When ignoring the bath-ink interactions, filament printing at a lower path speed (less than 10 mm/s) does not impose strict requirements on the support bath's τ_0 and t_c . As reported in the literature, τ_0 and t_c can be chosen within broader ranges of 1–100 Pa [15,22,35,41] and 0.2-0.5 s [15,25,42,43], respectively. However, when printing at an elevated path speed (e.g., 110 mm/s), the support bath must have a high τ_0 to stabilize filaments and a long t_c to fill the air gap behind the nozzle and maintain the filament morphology. This finding is consistent with the result in the published article [44]. Generally, t_c functions as the baseline to determine the suitability of the fluid for serving as a support bath. A relatively long t_c can facilitate the formation of well-defined filaments, such as swelling filament, equivalent diameter filament, stretched filament, etc. τ_0 decides the maximum path speed the support bath can suffer. Ink material with a higher η_0 shows better shape controllability. However, if a low-viscosity ink is selected, it is still feasible to tune the filament morphology by using a dispensing nozzle with a smaller inner diameter.

Supplementary material related to this article can be found online at

doi:10.1016/j.addma.2024.104353.

3.3. Evaluation of formed filaments

Based on the filament formation results summarized in Table S1, a position-shape-size (PSS) evaluation system is established and proposed to comprehensively assess the suitability of filaments for EIW, as shown in Fig. 4A. The flowchart to explain how to use this system is illustrated in Fig. 4B. First, filament position needs to be qualitatively evaluated. A qualified support bath must possess the yield stress in a specific range (as summarized in Table S2) to hold the deposited filaments *in situ*. Thus, all filaments can be stacked together based on the pre-defined trajectories to construct well-organized 3D structures. In a support bath with low or negligible τ_0 , sinking filaments are generated, leading to uncontrolled intra- and inter-layer filament fusion.

After that, it is necessary to qualitatively assess the filament shape from two aspects: overall shape and cross-sectional shape. Some filaments have irregular overall shapes that cannot be used for printing applications, including twisted filament, over-extruded filament, broken filament, discontinuous filament, and compressed filament. Their formation mechanisms are different from each other but are all dependent on the coupling effects between support bath, ink, and printing conditions. A set of overall-shape indicators, including filament surface flatness, straightness, and symmetricity, are also defined in Supporting Information S9 to quantitatively evaluate filaments, if needed. Several well-defined filaments in the published articles are collected and their surface flatness, straightness, as well as symmetricity, are calculated and summarized in Table S3, which are used as the references. For the welldefined filaments (e.g., stretched filament) in this work, the flatness indicators (i.e., σ_i and σ_i in Fig. S7) are at a low level of around 0.02, falling in the reference range (0.01-0.1). In addition, the similarities to evaluate the filament straightness and symmetricity are 88.90 % and 87.49 %, respectively, both falling in the reference ranges (> 74 % and 74-95 %). In contrast, an over-extruded filament has flatness indicators between 0.3 and 1 and similarities of around 57 % and 79 %, which greatly depart from the reference values, showing this filament possesses an unqualified overall shape.

Once the overall shape meets the requirement, the subsequent step is to evaluate the cross-sectional shape of the filament by measuring its key dimensions. For example, compressed filament usually has the crosssectional dimensions out of control along the ink extrusion direction (i.e., z direction in Fig. 2), making it challenging to achieve a high shape accuracy of printed 3D structures in this direction. Therefore, compressed filament should be avoided in EIW. Burred surface filament has a well-controlled overall shape but a slightly irregular cross-sectional shape. Although burs affect the surface quality of 3D structures, they may interact/entangle with each other to promote the inter-filament fusion. As a result, this type of filament has already been applied in freeform reversible embedding of suspended hydrogels (FRESH) to print human tissue and organ equivalents that do not have a high surface quality requirement [9,17,37]. The aspect ratio, as defined in Supporting Information S10, can be applied to quantitatively assess the cross section of filaments, if the qualitative evaluation is insufficient. As shown in Table S4, a representative compressed filament has an aspect ratio of around 0.5, much lower than both the summarized standards (> 0.7) as well as the aspect ratio of a swelling filament (0.89) in this work. As a result, its cross-sectional shape is out of control.

Finally, a quantitative evaluation needs to be performed on the filaments which pass the assessments of position and shape. These filaments include swelling filament, equivalent diameter filament, stretched filament, and shrunk filament. The first three types of filaments are observed in this work and their cross-sectional sizes (i.e., diameters) are mainly affected by the difference between v_{ink} and v_{path} as discussed above. Some key printing parameters, such as layer thickness and step distance, can be determined based on the measured diameter. Due to controllable cross-sectional size and stable longitudinal size,

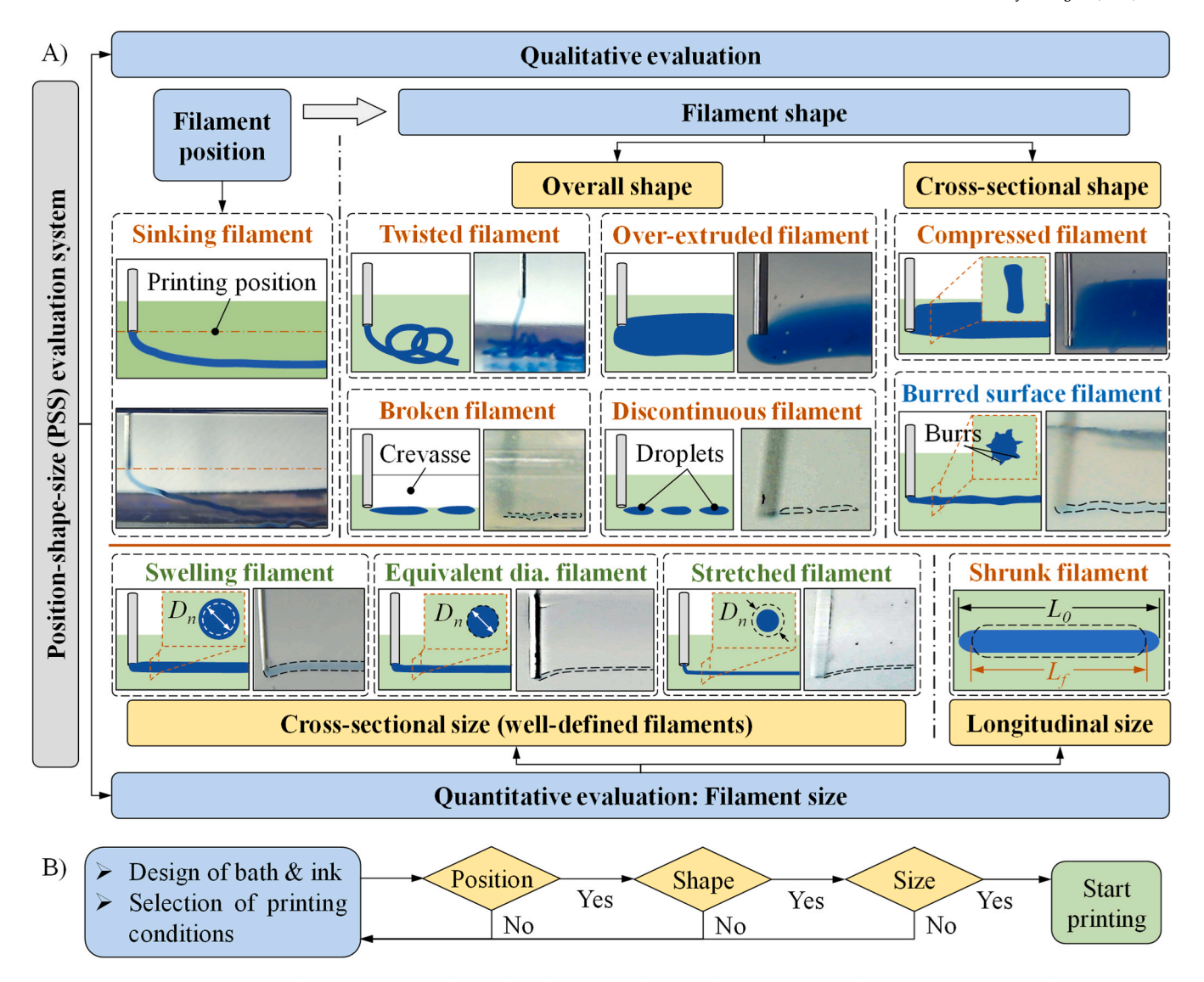


Fig. 4. A) Position-shape-size (PSS) evaluation system to qualitatively and quantitatively assess filaments for EIW applications. B) Flowchart to show how to use the evaluation system.

these filaments are categorized into well-defined filaments which are most commonly used in EIW [22,23,25]. The last type of filament occurs when the support bath and ink have the opposite hydrophilicity and hydrophobicity. For example, when printing an amphiphilic Pluronic F127 ink within a hydrophobic polydimethylsiloxane (PDMS)-fumed silica support bath, the existence of an immiscible ink-bath interface prevents the support bath from stably anchoring the extruded stretched filaments in place. Thus, the filaments slowly and uniformly shrink along the nozzle moving direction, causing the historical change of the longitudinal and radial sizes [38]. Although this type of filament is not recommended, it can still be used for EIW by either compensating the shrinkage in the part design stage [20] or rapidly solidifying the printed structure before observable shrinkage occurs [38].

3.4. Embedded ink writing of complex 3D structures

Two representative structures are designed, including a human nose and a human ear, to validate that the well-defined filaments evaluated by the PSS system can be used for 3D printing. To minimize the printing time, the support bath with high τ_0 and long t_c is selected, which is able to form well-defined filaments from both hydrogel inks at high path speeds. The nose and ear models (Fig. 5A1 and B1) are first sliced into

numerous layers. The printing trajectories of each layer are generated accordingly. Then, the dispensing nozzle moves within the support bath at 110 mm/s to rapidly deposit the hydrogel ink layer by layer according to the pre-defined trajectories. Due to the long t_c , the liquefied support bath material around the nozzle tip quickly and completely fills the crevasse behind the nozzle, as shown in Fig. 5A2. Additionally, the high τ_0 enables the deposited filaments to be stabilized in the support bath at the high path speed, making it feasible to achieve a liquid 3D structure with high resolution before undergoing the crosslinking process, as illustrated in Fig. 5B2.

Supplementary material related to this article can be found online at doi:10.1016/j.addma.2024.104353.

Because the hydrogel ink is composed of NaAlg and PEGDA, both ionic crosslinking and UV crosslinking can induce the solidification of printed structures. In this work, the UV radiation is applied first to photo crosslink the PEGDA component within the liquid nose and ear structures, as shown in Fig. 5A3 and B3, respectively. Then, the structures have sufficient mechanical stiffness to be collected from the support bath. Finally, the printed nose and ear are submerged in the calcium chloride bath to ionically crosslink the NaAlg component. After cleaning the residual support bath material on the surfaces, the nose and ear structures are achieved, which present good shape fidelity as shown in

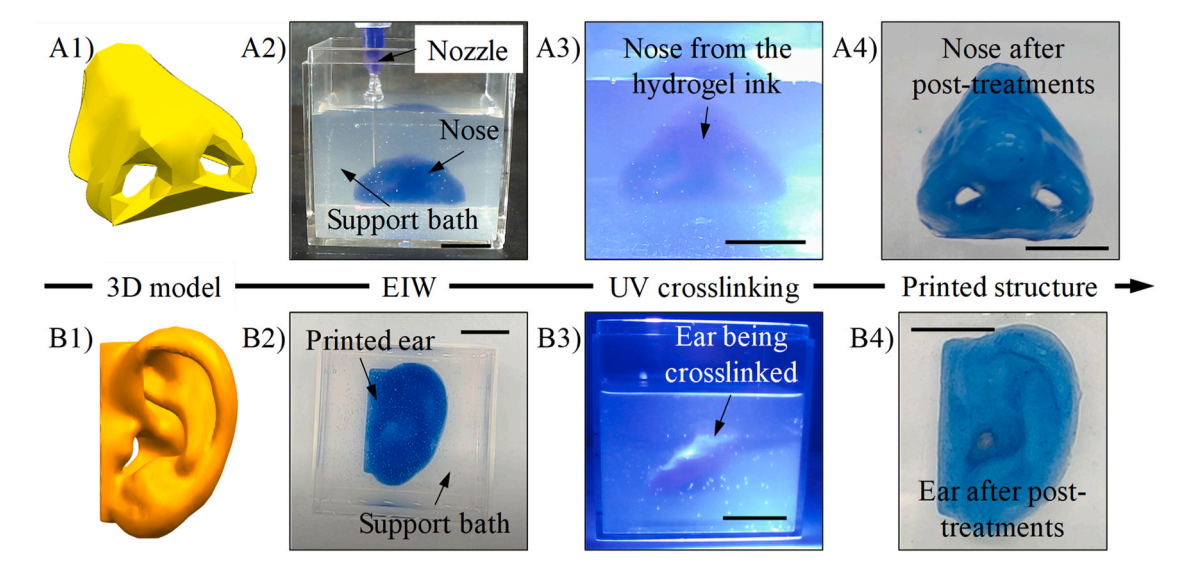


Fig. 5. EIW of complex 3D structures. 3D models of A1) human nose and B1) human ear. A2) Nose and B2) ear printing within the support bath with high τ_0 and long t_c at 110 mm/s. UV crosslinking of printed A3) nose and B3) ear in the support bath. A4) Nose and B4) ear structures after post-treatments. Scale bars: 15 mm for A) and 20 mm for B).

Fig. 5A4 and B4. The fabrication processes are recorded in Movies S6 and S7. The key dimensions are measured in Supporting Information S11 and S12. The relative errors are all less than 1 %, which validates the high accuracy of the structures made from the well-defined filaments.

4. Conclusion and future work

In this work, ten types of filaments are observed in different yield-stress support baths by embedded printing low- and high-viscosity hydrogel inks under various printing conditions. It is found that a relatively long t_c can facilitate the formation of well-defined filaments within a yield-stress support bath while τ_0 decides the maximum path speed the support bath can suffer. High τ_0 is necessary if high ν_{path} is targeted. In addition, increasing the ink's viscosity can help control the morphology of printed filaments. Using the proposed PSS system, a filament can be comprehensively evaluated in terms of position, shape, and size to determine whether it can be used for EIW or not. Integrating with the mechanism studies, a human nose and a human ear are successfully printed from the high-viscosity hydrogel ink within the support bath with high τ_0 and long t_c , which enables the formation of well-defined filaments at higher path speeds.

This work mainly focuses on experimentally explaining different filament formation mechanisms. It is noted that except τ_0 and t_c , other rheological parameters (e.g., shear moduli, viscosity, etc.) of yield-stress fluids also affect the filament formation in EIW. Analytical models will be established in the future to quantitatively describe the core physical phenomena, which will be integrated with machine learning to develop a physics-informed machine learning platform to accurately predict necessary filament information (i.e., position, shape, and size) based on the designed support bath and ink as well as selected operating conditions. In addition, two hydrophilic inks are printed into different hydrophilic support baths in this work, which makes the effects of interfacial tension on filament formation ignored. In the future, support baths and inks with opposite hydrophilicity and hydrophobicity will be used to print filaments in a large path speed range, which may lead to the generation of different filaments. Since the focus of this work is to experimentally explore the filament formation mechanisms in a broader path speed range, only one nanocomposite is selected to demonstrate its capability as a support bath for EIW of human nose and ear models. More printing experiments will be designed in the future with the emphasis placed on qualifying the functionality of other

nanocomposites for printing complex 3D structures.

CRediT authorship contribution statement

Weijian Hua: Writing – review & editing, Writing – original draft, Visualization, Methodology, Investigation, Formal analysis, Data curation, Conceptualization. Cheng Zhang: Writing – original draft, Visualization, Methodology, Investigation, Formal analysis, Data curation. Kellen Mitchell: Investigation, Formal analysis. Lily Raymond: Investigation. Ryan Coulter: Writing – review & editing. Erick Bandala: Writing – review & editing. Danyang Zhao: Writing – review & editing, Supervision, Funding acquisition. Yifei Jin: Writing – review & editing, Writing – original draft, Supervision, Project administration, Funding acquisition, Conceptualization.

Declaration of Generative AI and AI-assisted technologies in the writing process

During the preparation of this work, the authors did not used any AI or AI-assisted technologies. The authors reviewed and edited all content in this work and take full responsibility for the content of the publication.

Declaration of Competing Interest

The authors declare the following financial interests/personal relationships which may be considered as potential competing interests: Lily Raymond and Ryan Coulter reports financial support was provided by National Science Foundation. Danyang Zhao reports financial support was provided by National Key R&D Program of China. Danyang Zhao reports financial support was provided by National Natural Science Foundation of China. Yifei Jin reports financial support was provided by National Science Foundation. If there are other authors, they declare that they have no known competing financial interests or personal relationships that could have appeared to influence the work reported in this paper.

Data availability

Data will be made available on request.

Acknowledgment

Weijian Hua and Cheng Zhang contributed equally to this work. Lily Raymond acknowledges the support of the National Science Foundation Graduate Research Fellowship Program through NSHE sub-award number: AWD0002282-1937966. Ryan Coulter acknowledges the support of the National Science Foundation Graduate Research Fellowship Program through NSHE sub-award number: AWD01-00002282. Danyang Zhao acknowledges the support of the National Key R&D Program of China (2018YFA0703000) and the National Natural Science Foundation of China (52175289). Yifei Jin acknowledges the support of the National Science Foundation (OIA-2229004).

Appendix A. Supporting information

Supplementary data associated with this article can be found in the online version at doi:10.1016/j.addma.2024.104353.

References

- L. Zhou, J. Fu, Y. He, A review of 3D printing technologies for soft polymer materials, Adv. Funct. Mater. 30 (2020) 2000187, https://doi.org/10.1002/ adfm 202000187
- [2] J. Zhao, N. He, A mini-review of embedded 3D printing: supporting media and strategies, J. Mater. Chem. B. 8 (2020) 10474–10486, https://doi.org/10.1039/ d0tb01810b
- [3] J. Placone, A. Engler, Recent advances in extrusion-based 3D printing for biomedical applications, Adv. Healthc. Mater. 7 (2017), https://doi.org/10.1002/ adhm.201701161.
- [4] W. Hua, K. Mitchell, L. Raymond, B. Godina, D. Zhao, W. Zhou, Y. Jin, Fluid bath-assisted 3D printing for biomedical applications: from pre- to post printing stages, ACS Biomater. Sci. Eng. 7 (2021) 4736–4756, https://doi.org/10.1021/acsbiomaterials.1c00910.
- [5] R. Truby, M. Wehner, A. Grosskopf, D. Vogt, S. Uzel, R. Wood, J.A. Lewis, Soft somatosensitive actuators via embedded 3D printing, Adv. Mater. 30 (2018) 1706383, https://doi.org/10.1002/adma.201706383.
- [6] B. Sparrman, C. Pasquier, C. Thomsen, S. Darbari, R. Rustom, J. Laucks, K. Shea, S. Tibbits, Printed silicone pneumatic actuators for soft robotics, Addit. Manuf. 40 (2021) 101860, https://doi.org/10.1016/j.addma.2021.101860.
- [7] P. Wei, X. Yang, Z. Cao, X. Guo, H. Jiang, Y. Chen, M. Morikado, X. Qiu, D. Yu, Flexible and stretchable electronic skin with high durability and shock resistance via embedded 3D printing technology for human activity monitoring and personal healthcare, Adv. Mater. Technol. 4 (2019), https://doi.org/10.1002/ admt.201900315.
- [8] P. Raymundo-Pereira, N. Gomes, S. Machado, O. Oliveira, Wearable gloveembedded sensors for therapeutic drug monitoring in sweat for personalized medicine, Chem. Eng. J. 435 (2022) 135047, https://doi.org/10.1016/j. cei.2022.135047.
- [9] T. Hinton, Q. Jallerat, R. Palchesko, J. Park, M. Grodzicki, H. Shue, M.H. Ramadan, A.R. Hudson, A.W. Feinberg, Three-dimensional printing of complex biological structures by freeform reversible embedding of suspended hydrogels, Sci. Adv. 1 (2015) e1500758, https://doi.org/10.1126/sciadv.1500758.
- [10] M. Skylar-Scott, S. Uzel, L. Nam, J. Ahrens, R. Truby, S. Damarajuet, J.A. Lewis, Biomanufacturing of organ-specific tissues with high cellular density and embedded vascular channels, Sci. Adv. 5 (2019) eaaw2459, https://doi.org/ 10.1126/sciadv.aaw2459.
- [11] S. Duraivel, D. Laurent, D.A. Rajon, G.M. Scheutz, A. Shetty, B.S. Sumerlin, S. A. Banks, F.J. Bova, T.E. Angelini, A silicone-based support material eliminates interfacial instabilities in 3D silicone printing, Science 379 (2023) 1248–1252, https://doi.org/10.1126/science.ade4441.
- [12] Y. Li, Z. Wu, Y. Chen, S. Xian, Z. Hong, Q. Wang, P. Jiang, H. Yu, Y. Zhong, Multi-material embedded 3D printing for one-step manufacturing of multifunctional components in soft robotics, Addit. Manuf. (2024) 104178, https://doi.org/10.1016/j.addma.2024.104178.
- [13] T. Calais, N.D. Sanandiya, S. Jain, E. Kanhere, S.K. Kumar, R.C. Yeow, P.V. y Alvarado, Freeform liquid 3D printing of soft functional components for soft robotics, ACS Appl. Mater. Interfaces 14 (2021) 2301–2315, https://doi.org/10.1021/acsami.1c20209.
- [14] Z. Wang, B. Zhang, W. Cui, N. Zhou, Freeform fabrication of pneumatic soft robots via multi-material jointed direct ink writing, Macromol. Mater. Eng. 307 (2022) 2100813, https://doi.org/10.1002/mame.202100813.
- [15] T. Bhattacharjee, S. Zehnder, K. Rowe, S. Jain, R. Nixon, W. Sawyer, T.E. Angelini, Writing in the granular gel medium, Sci. Adv. 1 (2015) e1500655, https://doi.org/ 10.1126/sciadv.1500655.
- [16] Y. Jin, A. Compaan, W. Chai, Y. Huang, Functional nanoclay suspension for printing-then-solidification of liquid materials, ACS Appl. Mater. Interfaces 9 (2017) 20057–20066, https://doi.org/10.1021/acsami.7b02398.
- [17] E. Mirdamadi, J. Tashman, D. Shiwarski, R. Palchesko, A.W. Feinberg, FRESH 3D bioprinting a full-size model of the human heart, ACS Biomater. Sci. Eng. 6 (2020) 6453–6459, https://doi.org/10.1021/acsbiomaterials.0c01133.

- [18] A. Nelson, B. Kundukad, W. Wong, S. Khan, P. Doyle, Embedded droplet printing in yield-stress fluids, PNAS 117 (2020) 5671–5679, https://doi.org/10.1073/ pngs 1919363117
- [19] J. Muth, D. Vogt, R. Truby, Y. Mengüç, D. Kolesky, R. Wood, J.A. Lewis, Embedded 3D printing of strain sensors within highly stretchable elastomers, Adv. Mater. 26 (2014) 6307–6312, https://doi.org/10.1002/adma.201400334.
- [20] A. Grosskopf, R. Truby, H. Kim, A. Perazzo, J.A. Lewis, H. Stone, Viscoplastic matrix materials for embedded 3D printing, ACS Appl. Mater. Interfaces 10 (2018) 23353–23361, https://doi.org/10.1021/acsami.7b19818.
- [21] L. Friedrich, J. Seppala, Simulated filament shapes in embedded 3D printing, Soft Matter 17 (2021) 8027–8046, https://doi.org/10.1039/d1sm00731a.
- [22] L. Friedrich, R. Gunther, J. Seppala, Suppression of filament defects in embedded 3D printing, ACS Appl. Mater. Interfaces 14 (2022) 32561–32578, https://doi.org/ 10.1021/acsami.2c08047.
- [23] Y. Jin, W. Chai, Y. Huang, Printability study of hydrogel solution extrusion in nanoclay yield-stress bath during printing-then-gelation biofabrication, Mater. Sci. Eng. C. 80 (2017) 313–325, https://doi.org/10.1016/j.msec.2017.05.144.
- [24] Y. Jin, C. Liu, W. Chai, A. Compaan, Y. Huang, Self-supporting nanoclay as internal scaffold material for direct printing of soft hydrogel composite structures in air, ACS Appl. Mater. Interfaces 9 (2017) 17456–17465, https://doi.org/10.1021/ acsami.7b03613.
- [25] W. Hua, K. Mitchell, L. Kariyawasam, C. Do, J. Chen, L. Raymond, N. Valentin, R. Coulter, Y. Yang, Y. Jin, Three-dimensional printing in stimuli-responsive yieldstress fluid with an interactive dual microstructure, ACS Appl. Mater. Interfaces 14 (2022) 39420–39431, https://doi.org/10.1021/acsami.2c12465.
- [26] N. Diamantides, C. Dugopolski, E. Blahut, S. Kennedy, L. Bonassar, High density cell seeding affects the rheology and printability of collagen bioinks, Biofabrication 11 (2019) 045016, https://doi.org/10.1088/1758-5090/ab3524.
- [27] W. Zhou, H. Zhang, Y. Liu, X. Zou, J. Shi, Y. Zhao, Y. Ye, Y. Yu, J. Guo, Sodium alginate-polyethylene glycol diacrylate based double network fiber: rheological properties of fiber forming solution with semi-interpenetrating network structure, Int. J. Biol. Macromol. 142 (2020) 535–544, https://doi.org/10.1016/j.iibiomac.2019.09.125
- [28] W. Zhou, H. Zhang, Y. Liu, X. Zou, J. Shi, Y. Zhao, Y. Ye, Y. Yu, J. Guo, Preparation of calcium alginate/polyethylene glycol acrylate double network fiber with excellent properties by dynamic molding method, Carbohydr. Polym. 226 (2019) 115277, https://doi.org/10.1016/j.carbpol.2019.115277.
- [29] W. Xu, S. Jambhulkar, Y. Zhu, D. Ravichandran, M. Kakarla, B. Vernon, D.G. Lott, J.L. Cornella, O. Shefi, G. Miquelard-Garnier, Y. Yang, K. Song, 3D printing for polymer/particle-based processing: a review, Compos. B Eng. 223 (2021) 109102, https://doi.org/10.1016/j.compositesb.2021.109102.
- [30] S. Zhou, I.S. Tirichenko, X. Zhang, Y. Hong, H. Payne, P.J. Withers, F. Bouville, E. Saiz, Embedded 3D printing of microstructured multi-material composites, Matter (2023), https://doi.org/10.1016/j.matt.2023.10.031.
- [31] Y. Guan, Y. Xie, D. Qiu, House-of-cards" structures in silicone rubber composites for superb anti-collapsing performance at medium high temperature, RSC Adv. 6 (2016) 7970–7976, https://doi.org/10.1039/c5ra26937g.
- [32] K. Zhou, M. Dey, B. Ayan, Z. Zhang, V. Özbolat, M. Kim, V. Khristov, İ.T. Özbolat, Fabrication of PDMS microfluidic devices using nanoclay-reinforced Pluronic F-127 as a sacrificial ink, Biomed. Mater. 16 (2021) 045005, https://doi.org/ 10.1088/1748-605x/abe55e.
- [33] P. Desai, N. Jain, R. Sharma, P. Bahadur, Effect of additives on the micellization of PEO/PPO/PEO block copolymer F127 in aqueous solution, Colloids Surf. A Physicochem. Eng. Asp. 178 (2001) 57–69, https://doi.org/10.1016/s0927-7757 (00)00493-3.
- [34] A. Nelson, T. Cosgrove, Small-angle neutron scattering study of adsorbed Pluronic tri-block copolymers on laponite, Langmuir 21 (2005) 9176–9182, https://doi.org/ 10.1021/la050680p.
- [35] A. Compaan, K. Song, Y. Huang, Gellan fluid gel as a versatile support bath material for fluid extrusion bioprinting, ACS Appl. Mater. Interfaces 11 (2019) 5714–5726, https://doi.org/10.1021/acsami.8b13792.
- [36] V. Bertolino, G. Cavallaro, M. Merli, S. Milioto, F. Parisi, L. Sciascia, Effect of the biopolymer charge and the nanoclay morphology on nanocomposite materials, Ind. Eng. Chem. Res. 55 (2016) 7373–7380, https://doi.org/10.1021/acs.iecr.6b01816.
- [37] T.J. Hinton, A. Hudson, K. Pusch, A. Lee, A.W. Feinberg, 3D printing PDMS elastomer in a hydrophilic support bath via freeform reversible embedding, ACS Biomater. Sci. Eng. 2 (2016) 1781–1786, https://doi.org/10.1021/acsbiomaterials.6b00170.
- [38] W. Hua, K. Mitchell, L. Raymond, N. Valentin, R. Coulter, Y. Jin, Embedded 3D printing of PDMS-based microfluidic chips for biomedical applications, J. Manuf. Sci. Eng. 145 (2022), https://doi.org/10.1115/1.4055323.
- [39] M. Taghizadeh, A. Taghizadeh, M. Yazdi, P. Zarrintaj, F. Stadler, J. Ramsey, S. Habibzadeh, S.H. Rad, G. Naderi, M.R. Saeb, M. Mozafari, U.S. Schubert, Chitosan-based inks for 3D printing and bioprinting, Green. Chem. 24 (2022) 62–101, https://doi.org/10.1039/d1gc01799c.
- [40] M. Saadi, A. Maguire, N. Pottackal, S. Thakur, M. Ikram, A. Hart, P.M. Ajayan, M. M. Rahman, Direct ink writing: a 3D printing technology for diverse materials, Adv. Mat. 34 (2022), https://doi.org/10.1002/adma.202108855.
- [41] Q. Li, Z. Gao, J. Yin, P. Liu, H. Yang, L. Shen, H. Zhou, Regulable supporting baths for embedded printing of soft biomaterials with variable stiffness, ACS Appl. Mater. Interfaces 14 (2022) 41695–41711, https://doi.org/10.1021/acsami.2c09221.
- [42] L. Raymond, W. Hua, N. Valentin, R. Coulter, E. Bandala, K. Leong, J. Okaikoi, Y. Jin, Coaxial nozzle-assisted embedded 3D printing of single-layered channels

- within a yield-stress matrix bath, J. Manuf. Sci. Eng. 146 (2023), https://doi.org/
- [43] Y. Jin, K.J. Song, N. Gellermann, Y. Huang, Printing of hydrophobic materials in fumed silica nanoparticle suspension, ACS Appl. Mater. Interfaces 11 (2019) 29207–29217, https://doi.org/10.1021/acsami.9b07433.
- [44] K. LeBlanc, S. Niemi, A. Bennett, K. Harris, K. Schulze, W. Sawyer, C.R. Taylor, T. E. Angelini, Stability of high speed 3D printing in liquid-like solids, ACS Biomater. Sci. Eng. 2 (2016) 1796–1799, https://doi.org/10.1021/acsbiomaterials.6b00184.